

# Application of the FRADO model of BLR formation to the Seyfert galaxy NGC 5548 and the first step toward determining the Hubble constant

Vikram Kumar Jaiswal<sup>1</sup>, Raj Prince<sup>1,2</sup>, Ashwani Pandey<sup>1,3</sup>, Mohammad Hassan Naddaf<sup>4</sup>, Bożena Czerny<sup>1</sup>, Swayamtrupta Panda<sup>5,\*</sup>, Amit Kumar Mandal<sup>1</sup>, and Francisco Pozo Nuñez<sup>6</sup>

<sup>1</sup> Center for Theoretical Physics, Polish Academy of Sciences, Al. Lotników 32/46, 02-668 Warsaw, Poland

<sup>2</sup> Department of Physics, Institute of Science, Banaras Hindu University, Varanasi-221005, India

<sup>3</sup> Department of Physics and Astronomy, University of Utah, Salt Lake City, UT 84112, USA

<sup>4</sup> Institut d’Astrophysique et de Géophysique, Université de Liège Allée du six août 19c, B-4000 Liège (Sart-Tilman), Belgium

<sup>5</sup> International Gemini Observatory/NSF NOIRLab, Casilla 603, La Serena, Chile

<sup>6</sup> Astroinformatics, Heidelberg Institute for Theoretical Studies, Schloss-Wolfsbrunnengasse 35, 69118 Heidelberg, Germany

## ABSTRACT

*Context.* The dynamical and geometric structures of the Broad Line Region (BLR), along with the origins of continuum time delays in active galaxies, remain topics of ongoing debate.

*Aims.* In this study, we aim to reproduce the observed broadband spectrum, the H $\beta$  line delay, and the continuum time delays using our newly developed model for the source NGC 5548.

*Methods.* We adopt the standard accretion disk model, with the option of an inner hot flow, and employ the lamp-post model to account for disk irradiation. Additionally, we model the BLR structure based on radiation pressure acting on dust. The model is parameterized by the black hole mass (which is fixed), the accretion rate, the viewing angle, the height of the lamp-post, the cloud density, and the cloud covering factor. The resulting continuum time delays arise from a combination of disk reprocessing and the reprocessing of a fraction of radiation by the BLR.

*Results.* Our model reasonably reproduces the observed broad-band continuum, the H $\beta$  time delay, and the continuum inter-band time delays measured during the observational campaign. When the accretion rate is not constrained by the known distance to the source, our approach allows for a direct estimation of the distance. The resulting Hubble constant,  $H_0 = 79.8^{+5.5}_{-16.4}$  km s<sup>-1</sup> Mpc<sup>-1</sup>, represents a significant improvement over the findings of Cackett et al. (2007).

*Conclusions.* This pilot study demonstrates that, with sufficient data coverage, it is possible to disentangle the time delays originating from the accretion disk and the BLR. This paves the way for effectively using inter-band continuum time delays as a method for determining the Hubble constant. Additionally, the findings provide strong support for the adopted model for the formation of the H $\beta$  line.

**Key words.** Accretion, accretion disks, Galaxies: active

## 1. Introduction

Seyfert 1 galaxy NGC 5548 is one of the most extensively observed active galactic nuclei (AGNs). Its brightness, relatively close distance, and significant variability made it an early candidate for studying the inner, unresolved structure of an active nucleus (e.g., Clavel et al. 1991; Peterson et al. 1991; Krolik et al. 1991; Rokaki et al. 1993). Among the various wavelengths, X-ray variability is the fastest, likely originating from the most compact region near the black hole. The reprocessing of this X-ray emission at longer wavelengths, observed through light echo studies, provides insights into the structure and dynamics of the surrounding material, a technique known as reverberation mapping (RM) (Blandford & McKee 1982; Peterson 1993). RM has been widely applied to AGNs (Sergeev et al. 2005; McHardy et al. 2014; Mudd et al. 2018; Homayouni et al. 2019; Yu et al. 2020; Guo et al. 2022), particularly in studies of continuum variability, which is believed to arise from the irradiated accretion disk. The simple standard disk model of Shakura & Sunyaev

(1973) predicts that the time delays ( $\tau$ ) should scale with wavelength ( $\lambda$ ) as  $\tau \propto \lambda^{4/3}$ . While observational results have roughly confirmed this trend, they have not matched the predicted normalization, as observed delays continue to exceed theoretical expectations (e.g. Cackett et al. 2007; Shappee et al. 2014; Kokubo 2018; Guo et al. 2022). This discrepancy, known as the accretion disk size problem, was first recognized in optical microlensing studies of gravitationally lensed quasars (Morgan et al. 2010) and remains an ongoing challenge in our understanding of AGN accretion disk structure.

The central components of AGNs include a massive black hole, a compact X-ray emitting region, a relatively cold Keplerian accretion disk, and the Broad Line Region (BLR) (see, e.g., Krolik 1999, for a basic compendium). The Keplerian disk serves as the primary source of continuum emission, while the BLR predominantly produces broad emission lines, along with a minor contribution to the continuum. In terms of spatial extent, the innermost regions of the accretion disk span approximately 10–100  $r_g$ , whereas the BLR extends outward to nearly 1000  $r_g$ .

\* Gemini Science Fellow

Recent intensive RM campaigns (Edelson et al. 2015; De Rosa et al. 2015; Fausnaugh et al. 2016; Pei et al. 2017; Horne et al. 2021; Lu et al. 2022) have significantly advanced our understanding of AGN nuclear structure. These studies have revealed that the observed optical continuum is not solely emitted by the accretion disk. Korista & Goad (2001) first noted that radiation reprocessed by the BLR contributes not only to the formation of emission lines but also to the diffuse continuum emission. This finding was later confirmed by Fausnaugh et al. (2016) and further emphasized by Cackett et al. (2021); Netzer (2022), who demonstrated that the diffuse BLR contribution can significantly dominate the measured continuum time delays. This effect poses challenges for using continuum time delays as a method to determine the Hubble constant,  $H_0$ , as originally proposed by Collier et al. (1999). For instance, Cackett et al. (2007) derived an  $H_0$  value of  $15 \pm 3 \text{ km s}^{-1} \text{ Mpc}^{-1}$ ; however, at the time, not all aspects of the physical mechanisms driving continuum time delays were fully understood.

This paper aims to test a specific model of BLR formation based on radiation pressure acting on dust in disk regions where the disk atmosphere temperature falls below the sublimation threshold. This model, known as the Failed Radiatively Accelerated Dusty Outflow (FRADO), was proposed to explain the vertical rise of material responsible for low-ionization lines, such as  $H\beta$  (Czerny & Hryniewicz 2011; Naddaf et al. 2021; Naddaf & Czerny 2022). In this study, we investigate the reprocessing of central radiation through a combination of two reprocessors: the Keplerian disk and the BLR, using the BLR response derived from the FRADO model. This approach provides a three-dimensional distribution of BLR clouds, which we then combine with a spectral shape model of the BLR generated using the CLOUDY code (version 23.00; Chatzikos et al. 2023). We fit this model to the observed spectrum and time delays of NGC 5548 and evaluate its potential for determining the distance to the source and the Hubble constant.

The structure of this paper is as follows. In Section 2, we describe the data used for fitting. Section 3 outlines our methodology, which involves generating the response function of the accretion disk using the lamp-post model and incorporating the BLR contribution via FRADO and CLOUDY to estimate the combined time delays. Section 4 presents the results obtained from different models, detailing the simultaneous fitting of the time lag and spectral energy distribution (SED) while assessing the strengths and limitations of each approach. Finally, in Section 5, we estimate the luminosity distance based on our best-fitting model.

## 2. Spectral shape and continuum time delay data of NGC 5548

NGC 5548 ( $z = 0.01651$ ) is one of the most extensively studied AGNs across multiple wavelengths. It was the primary target of the AGN Watch international collaboration (Peterson et al. 2002), which began investigating its emission line variability as early as 1987. Over the years, its optical and UV variability has been the subject of numerous studies (Peterson et al. 1991; Korista et al. 1995; Peterson et al. 1992, 2002, 2004). Observations from both ground-based and space-based telescopes have provided critical insights into accretion disk dynamics and emission line variability. Notably, optical variability in both the continuum and emission lines was first reported by de Vaucouleurs & de Vaucouleurs (1972) in the 1970s, while early UV observations commenced in 1988 with the International Ultraviolet Explorer (IUE; Ulrich & Boisson 1983). More recently, intensive

multi-wavelength monitoring campaigns (Edelson et al. 2015; De Rosa et al. 2015; Fausnaugh et al. 2016; Pei et al. 2017; Horne et al. 2021; Lu et al. 2022) have significantly deepened our understanding of the source.

These studies have revealed that the measured continuum time delays do not follow a simple power-law trend. Instead, they show clear evidence of interaction with an extended BLR, where different emission lines originate. Consequently, these delays are often approximated by mean time delays, though some emission line delay profiles exhibit double-peaked features. This complexity opens up new avenues for testing specific models of the BLR structure and response.

In this study, we utilize the broad-band SED and global parameters from Mehdipour et al. (2015), covering the period from 2013 to 2014. The broad-band SED, corrected for internal extinction, starlight contamination, the Balmer continuum, and the Fe II pseudo-continuum, was first presented by Mehdipour et al. (2015). Subsequently, Kubota & Done (2018) fitted this spectrum to an AGN spectral model, revealing that only the outermost part of the accretion flow corresponds to a standard disk. Their results further indicated that the optical/UV emission primarily originates from a region dominated by the warm corona (see their Figure 4).

Therefore, to systematically model the observed inter-band continuum time delays, we propose a step-by-step approach. First, we assume a standard accretion disk model (Model A). Next, we consider an alternative scenario (Model B) based on the spectral decomposition proposed by Kubota & Done (2018), in which optical/UV variability arises solely from the reprocessing of X-rays in the outer cold disk. In this case, the warm corona, with a temperature of approximately  $\sim 10^6 \text{ K}$ , is too optically thick to absorb and re-emit incident hard X-rays in the UV/X-ray bands, although it still contributes to the UV continuum. Finally, we introduce Model C, a new spectral decomposition based on Figure 5 of Mehdipour et al. (2015). Since the nature of disk reprocessing may strongly depend on the physical properties of the accretion disk, we also conduct a detailed re-analysis of the SED of the source. The disk parameters used for Models A, B, and C are summarized in Table 1.

To test these models, we utilize the time delay data from Fausnaugh et al. (2016), obtained during the STORM campaign from December 2013 to August 2014. This campaign integrated optical light curves data from 16 ground-based observatories, across the  $B, V, R, I$  filters, as well as the SDSS  $-u, g, r, i, z$  filters, coupled with ultraviolet data from the Hubble Space Telescope (HST) and Swift instruments. The inter-band time delays were measured relative to the HST light curve at  $1367 \text{ \AA}$ , providing a crucial dataset for evaluating the proposed disk reprocessing scenarios.

## 3. Method

Understanding the origin of continuum time delays in AGNs is crucial for probing the structure of the central engine and its surrounding medium. However, fitting these delays solely as a result of accretion disk reprocessing has often led to the so-called disk-size problem, as discussed earlier. Motivated by previous studies (Korista & Goad 2001; Netzer 2022; Jaiswal et al. 2023; Beard et al. 2025), we extend this framework by considering the reprocessing of central flux by both the accretion disk and the BLR medium. Given our twofold motivation, we adopt a theoretical modeling approach that accounts for all relevant aspects. This allows us not only to test the BLR model we employ but also

to explore the determination of the Hubble constant, as the relatively small number of model parameters enables us to treat the luminosity distance as an unknown parameter.

Building on this foundation, our model of an active nucleus comprises multiple key components: a standard accretion disk in the outer parts of the flow, a warm comptonizing corona, and a hot corona in the inner parts of the flow, the BLR region, and the contribution of the host galaxy to the total spectrum. In the following sections, we examine each of these components in detail.

### 3.1. Hot and warm corona

The hot corona, responsible for hard X-ray emission, was modeled by [Mehdipour et al. \(2015\)](#). In our approach, we adopt the proposed power-law shape and normalization for the observed spectrum when fitting the warm corona. However, we neglect the contribution of hard X-rays to the optical/UV part of the spectrum.

Unlike [Mehdipour et al. \(2015\)](#), we model the warm corona with a different approach. In our framework, the inner and outer radii of the warm corona are treated as parameters. The outer radius of the warm corona coincides with the inner radius of the standard (outer) disk. The Comptonization process in the warm corona is computed using the analytical formulae from [Sunyaev & Titarchuk \(1980\)](#) and is parameterized by the optical depth and electron temperature. Since the warm corona covers the inner disk, we do not assume a single temperature for the soft photons. Instead, we determine the temperature of the underlying cold disk at each radius and adjust it by the Comptonization amplification factor. These calculations are performed iteratively, ensuring that the soft photon temperature spans a continuous range while preserving the total energy from the accretion flow. This methodology aligns more closely with the approach of [Kubota & Done \(2018\)](#). The computational code used for this purpose was originally presented in [Czerny et al. \(2003\)](#).

Additionally, we do not include irradiation of the warm corona by hard X-rays, as the high temperature and large optical depth of the warm corona would cause the incident radiation to be predominantly scattered rather than absorbed and reprocessed. Consequently, no significant thermalization is expected, although some high-ionization lines, such as iron lines in the X-ray spectrum, may still be present ([Petrucci et al. 2020](#); [Baltayne et al. 2024](#)).

### 3.2. Cold disk reprocessing

The irradiating flux is thermalized only in the outer, cold regions of the standard accretion disk. To further explore this process, we simulate the lamp-post model to generate the disk's response function, assuming a pulse duration from the corona of 0.05 days. In this simulation, we exclude corrections for general relativity and energy-dependent reflection effects, as introduced by [Kammoun et al. \(2023, 2024\)](#); [Papoutsis et al. \(2024\)](#), to maintain a relatively simple code suitable for data fitting. As a result, the incident radiation from the corona is assumed to be fully absorbed by the disk, leading to a localized increase in temperature.

To accurately model the disk structure, we employ a non-uniform radial grid extending from the innermost stable circular orbit ( $R_{\text{isco}}$ ) to the outer disk radius ( $R_{\text{out}}$ ). The radial grid spacing follows the relation  $dR = 0.085 \times \left(\frac{R}{R_{\text{isco}}}\right)^{0.85}$ , where  $R$  is the radial distance from the central source in units of gravitational radius ( $r_g$ ). For each radial position, the azimuthal angle  $\phi$  is sampled using the relation  $d\phi = \frac{1.5700}{N_{\text{div}}}$ , where  $N_{\text{div}} = 3800$  ensures suf-

ficient resolution across the entire radial range. The surface element for each  $(R, \phi)$  coordinate is defined as  $ds = R \cdot dR \cdot d\phi$  in units of  $r_g^2$ . To facilitate further calculations, we convert  $(R, \phi)$  into Cartesian coordinates, assuming a geometrically thin disk with negligible height.

For each  $(x, y)$  coordinate, we compute the total time delay,  $\tau_{\text{total}}(x, y)$ , as the sum of two components: the delay from the corona to the disk,  $\tau_d(R)$ , and the delay from the disk to the plane intersecting the equatorial plane at  $R_{\text{out}}, \phi = 0$ , denoted as  $\tau_{\text{do}}(x, y)$ . The delay is influenced by key parameters, including the corona height ( $h$ ), the inclination angle of the system, and the black hole mass. By default, we assume a cold Keplerian disk extending down to the ISCO at  $6 r_g$ , with an outer radius of  $10^4 r_g$ . However, we also consider cases with different inner and outer radii, which can be set through the parameter  $r_{\text{in}}$ .

For a given delay, we calculate the flux with only a non-irradiated disk and a combination of disk emission and irradiation.

$$F_{\text{non-irradiated}}(r, t + \tau_d(r)) = \left( \frac{3GM\dot{M}}{8\pi r^3} \left( 1 - \sqrt{\frac{r_{\text{in}}}{r}} \right) \right) \quad (1)$$

$$F_{\text{disk+irradiation}}(r, t + \tau_d(r)) = \left( \frac{3GM\dot{M}}{8\pi r^3} \left( 1 - \sqrt{\frac{r_{\text{in}}}{r}} \right) \right) + \left( \frac{L_x(t)h}{4\pi r^3} \right) \quad (2)$$

$$T_{\text{disk}}(r, t + \tau_d(r)) = \left[ \left( \frac{3GM\dot{M}}{8\pi r^3 \sigma_B} \left( 1 - \sqrt{\frac{r_{\text{in}}}{r}} \right) \right) \right]^{\frac{1}{4}} \quad (3)$$

$$T_{\text{eff}}(r, t + \tau_d(r)) = \left[ \left( \frac{3GM\dot{M}}{8\pi r^3 \sigma_B} \left( 1 - \sqrt{\frac{r_{\text{in}}}{r}} \right) \right) + \left( \frac{L_x(t)h}{4\pi r^3 \sigma_B} \right) \right]^{\frac{1}{4}} \quad (4)$$

We calculate the blackbody emission both based solely on the disk temperature and from the combined effects of the disk and irradiation. To obtain the final emission, we subtract the contribution from the disk.

To compute the full spectrum for a specific differential area, we use Planck's formula and store the results in a photon table, represented as a 2D matrix denoted as  $\mathbf{P}(\mathbf{t}', \lambda)$ . This involves applying the calculated time delay corresponding to the disk position and wavelength. Each element in the photon table represents a unique delay and wavelength  $\lambda$ , with the  $\lambda$  values ranging from 1000 to 10000 Å and selected using a logarithmic scale grid for simulation. We also introduce a color correction as a free parameter of the model.

Next, we generate the response function by sending a very short light pulse of  $\Delta t = 0.05$  days duration and normalizing the result by the incident bolometric luminosity. This is expressed by the following equation:

$$\psi(t, \lambda) = \frac{1}{\Delta t L_x} \int_{S_{\text{disk}}} B_\lambda(T_{\text{eff}}(r(t' - \tau_{\text{do}}(x, y)))) ds. \quad (5)$$

The time delay in the disk has been described previously by [Jaiswal et al. \(2023\)](#). Our adopted method, while simpler than the approaches presented by [Kammoun et al. \(2021b\)](#) and [Kammoun et al. \(2021a\)](#), which include corrections for general relativity and disk albedo, is sufficiently accurate for the current purpose.

### 3.3. BLR structure and reprocessing

To introduce the contribution from the BLR, we first describe its properties. In this study, we do not parameterize the structure of the BLR using arbitrary numbers or functions; instead, we calculate it based on the FRADO model, which was qualitatively proposed by Czerny & Hryniewicz (2011) and has been further developed in several subsequent studies (Czerny et al. 2017; Naddaf et al. 2021; Naddaf & Czerny 2022; Naddaf et al. 2023; Naddaf & Czerny 2024). Specifically, we utilize the code from Naddaf et al. (2021), which provides a detailed numerical description of the wavelength-dependent cross-section for dusty particles. According to this model, radiatively dust-driven pressure lifts the clouds from the disk surface, while preserving their angular momentum derived from the Keplerian motion of the disk surface. As a cloud is lifted, it becomes increasingly illuminated by the inner parts of the disk. However, if the cloud becomes too hot, the dust evaporates, allowing the cloud to continue its motion along a ballistic orbit. The global parameters of the model, such as black hole mass, Eddington rate, and metallicity, govern the behavior of the BLR. For lower black hole masses, lower Eddington ratios, and lower metallicities, the clouds form a failed wind, while in the opposite case, a fraction of the clouds may form an escaping wind. Hence, we emphasize that the inner and outer radii of the BLR, along with the statistical distribution of the clouds, are governed by global parameters such as the black hole mass and the Eddington ratio.

With knowledge of the global parameters of the source, we can determine the 3-D locations of statistically representative clouds within the BLR. The code calculates 3-D trajectories of clouds launched from the disk. As described in Naddaf et al. (2021), clouds are then located at these trajectories proportionally to time they spent at each part of the trajectory. This information is then combined with the emissivity law for specific emission lines, particularly low-ionization lines such as H $\beta$ , Mg II, or Fe II. In our model, we assume that the emissivity weight of each cloud is influenced by its distance from the central disk: clouds closer to the center receive more radiation, resulting in a higher emissivity weight, while clouds farther away receive less radiation, leading to a lower weight, as defined in equation 6:

$$w \propto d^{-2}, \quad (6)$$

where  $d$  is the distance of a cloud from the center. This scaling of the emissivity, which inversely depends on the square of the distance, neglects the local efficiency of converting incident flux into BLR spectrum. However, since our model does not yet predict the local density, this simplification is reasonable at this stage of development. Later in the model, we fix the local density of the cloud at  $10^{11} \text{ cm}^{-3}$ . For convenience, the value  $4900 r_g$  serves as a reference.

By supplementing the cloud distribution with emissivity, we can determine the emission line profile for any viewing angle relative to the observer, as demonstrated in Naddaf & Czerny (2022). Next, we focus on calculating the response function  $\psi_{BLR}(t)$  for the BLR based on this distribution. This is accomplished by calculating the time delays for each representative cloud as observed, using a method analogous to that applied for disk emission. At this stage, we assume that the emissivity of the clouds is universal, though wavelength-dependent, which is determined through photoionization calculations for a representative cloud.

### 3.4. Photoionization calculations using CLOUDY

To determine the BLR spectral shape, we perform photoionization calculations using the code CLOUDY, version C23.00 (Chatzikos et al. 2023). In these computations, we simplify the 3-D cloud distribution by replacing the entire ensemble of clouds with a single representative cloud, positioned at the radius inferred from the time delay. For the analysis at this established distance, we adopt an incident radiation luminosity of  $\log L$  (erg/s) = 44, a BLR distance from the central source of  $\log r$  (cm) = 16, a constant hydrogen gas density of  $\log n_H$  ( $\text{cm}^{-3}$ ) = 11, and a column density of  $\log N_H$  ( $\text{cm}^{-2}$ ) = 23.5, following the prescriptions of (Korista & Goad 2001; Panda et al. 2022). We assume solar metallicity and neglect turbulence in the medium.

The shape of the incident SED is taken from the file "NGC5548.sed" available in the CLOUDY database, which corresponds to the SED derived by Mehdipour et al. (2015). Their study estimated the starlight contribution to NGC 5548 using HST observations, providing a well-constrained incident SED that we adopt for our calculations. The resulting BLR emissivity profile,  $\epsilon(\lambda)$ , is then incorporated into the final delay model. When we later account for the assumption of an unknown luminosity distance, the irradiating flux is adjusted accordingly to ensure consistency with the observed hard X-ray flux.

Since CLOUDY does not compute higher-order Balmer lines, we incorporate a scaled component into the spectrum, following the method of Kovačević et al. (2014). This modification improves the spectral fit, as demonstrated in Pandey et al. (2024), though it only affects the wavelength range between 3646Å and 4000Å in the rest frame.

### 3.5. Starlight contribution

The starlight contribution in NGC 5548 was estimated by Mehdipour et al. (2015), and we adopt the same level in some of our models. However, in other models, we allow for flexibility in adjusting the starlight level. To represent the starlight profile, we use the template of an Sa galaxy from Kinney et al. (1996), which is available in the Kinney-Calzetti Spectral Atlas<sup>1</sup>.

### 3.6. Combined time delay and NGC 5548 data fitting

After analyzing each component of the central regions assumed in our model for NGC 5548, we derive the final response function by incorporating both disk reprocessing and BLR contributions, as expressed in the following equation

$$\psi(\lambda, t) = (1 - f_{BLR})\psi_d(\lambda, t) + f_{BLR} \times \epsilon(\lambda) \int_{t_0}^{t_{max}} \psi_d(\lambda, t')\psi_{BLR}(t')dt'. \quad (7)$$

where the parameter  $f_{BLR}$  defines the BLR fraction contributing to the continuum time delay.

We generate response functions for 100 wavelengths, covering the range from 1000 Å to 10000 Å. Using these response functions, we then compute the time delay at each wavelength using the following equation:

$$\tau(\lambda) = \frac{\int t\psi(t, \lambda)dt}{\int \psi(t, \lambda)dt}. \quad (8)$$

<sup>1</sup> <https://www.stsci.edu/hst/instrumentation/reference-data-for-calibration-and-tools/astronomical-catalogs/the-kinney-calzetti-spectral-atlas>

**Table 1.** Parameters utilized in modeling the delay and spectral energy distribution (SED) of NGC 5548.

Parameters	Model A	Model B	Model C
(1)	(2)	(3)	(4)
Black Hole Mass	$5 \times 10^7$	$5.5 \times 10^7$	$5 \times 10^7$
Corona Height	20	43	32
Inclination Angle	40	45	40
Warm corona Inner Radius	-	43	6
Warm Corona Temperature	-	$1.98 \times 10^6$	$5.97 \times 10^6$
Warm corona optical depth/Photon index	-	2.28	21.5
Inner Cold Disk Radius	35	151	90
Outer Cold Disk Radius	10000	282	10000
Color Correction	2.4	1.0	1.0
BLR Contribution( $f_{BLR}$ )	12%	40%	36%
Lamp Luminosity	$1.26 \times 10^{44}$	$1.247 \times 10^{44}$	$9.52 \times 10^{43}$
Eddington Ratio	0.02	0.027	0.015

**Note.** Columns are (1) name of the parameters used in the model. Black hole mass in unit of  $M_\odot$ , corona height in unit of  $r_g$ , inclination angle in degree, inner disk radius and outer disk radius in  $r_g$ , lamp luminosity in  $erg\ s^{-1}$ , (2) parameter values for Model A (3) parameter values for Model B, (4) parameter values for Model C. Warm corona optical depth or a photon index are alternative (equivalent) parameters of Comptonization models.

To fit the data of NGC 5548, we utilize all the parameters listed in Table 1, integrating the contributions from both the disk and the BLR as described in equation 7.

When searching for the optimal solution, we impose constraints from both the observed SED and the measured time delays. Specifically, we incorporate all 17 available time delay measurements and select 16 representative points, evenly distributed across the entire observed SED range. To systematically evaluate and compare different solutions, we integrate these constraints into a unified criterion:

$$\chi^2 = \sum \frac{(O_i - E_i)^2}{(\delta O_i)^2}, \quad (9)$$

where  $O_i$  = observed data,  $\delta O_i$  = is the error in observed data, and  $E_i$  = value from the model.

## 4. Results

In this section we concentrate on testing the FRADO model against the spectral and time-delay data for NGC 5548. We fix the mass of the central black hole and the bolometric luminosity in our analysis. We assume that the distance to the source is known, and corresponds to the source redshift. The issue of the Hubble constant determination will be addressed separately in Section 5.

### 4.1. BLR properties from FRADO

The global model parameters adopted for NGC 5548, combined with the assumption of a dust sublimation temperature of 1500 K, allow us to uniquely determine the structure of the BLR. Notably, the FRADO model is specifically applicable to low-ionization lines such as  $H\beta$ , Mg II, and Fe II. In this framework, the cloud positions within the BLR are determined by the FRADO model, with parameters relevant to NGC 5548: a black hole mass of  $M_{BH} = 5 \times 10^7 M_\odot$ , an Eddington ratio of 0.02, and an assumed metallicity 5 times solar.

We present the distribution of clouds forming the BLR in NGC 5548 in Figure 1. The upper panel presents the overall 3-D structure, revealing a complex cone-like configuration where

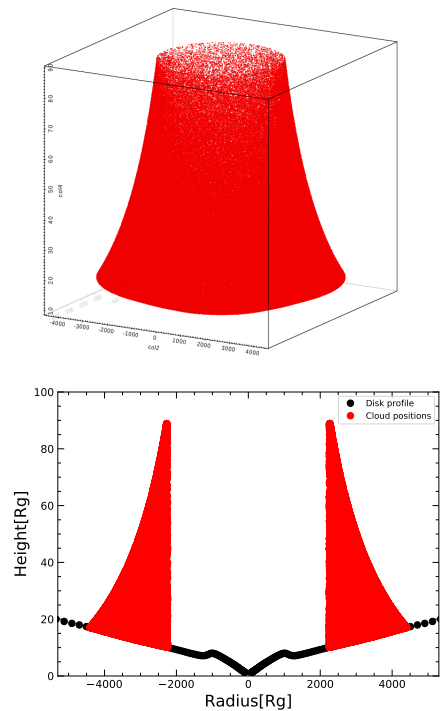


**Fig. 1.** Upper panel: 3-D plot of cloud positions from FRADO model,  $M_{BH} = 5 \times 10^7 M_\odot$ ,  $L/L_{Edd} = 0.02$ , metallicity  $Z = 5$  in solar units. The axes are in units of  $r_g$ . Bottom panel: a cross-section of cloud positions for  $y > -300r_g$  and  $y < 300r_g$ . Clouds form a geometrically thin complex layer above the disk.

no clouds escape to infinity due to the low Eddington rate. The lower panel provides a cross-section of this distribution, with the black line marking the thickness of the underlying Keplerian disk. This disk structure accounts for the effects of radiation pressure and opacity, as described by Różańska et al. (1999), both of which play a crucial role in shaping its complex geometry. A notable feature is the abrupt change in disk height, cor-

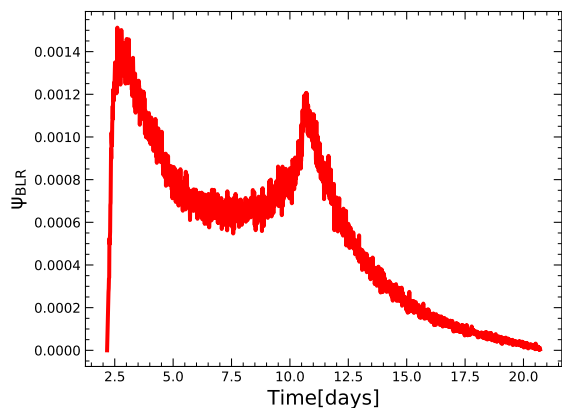


**Fig. 2.** BLR response function for model shown in Figure 1, generated for inclination angle 40 degrees.

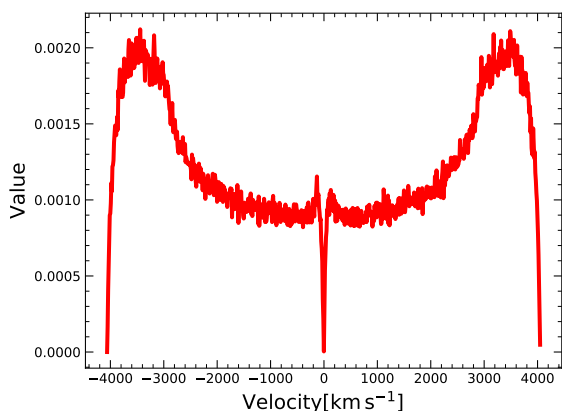


**Fig. 3.** Line profile generated by the FRADO model using the parameters from Figure 1.

responding to the transition from the inner radiation pressure-dominated region to the outer gas-dominated region, which significantly impacts the cooling efficiency of the disk and its overall structure.

In this model, clouds are launched from the disk surface but remain relatively close to it, with the ratio of vertical height ( $z$ ) to radial distance ( $r$ ) staying below 5%. This limited height is a direct consequence of the low Eddington ratio, giving the BLR a geometry that closely resembles a puffed-up disk surface. The  $z/r$  ratio peaks near the inner edge of the BLR, which is defined by the dust sublimation temperature at approximately  $\sim 2260 r_g$ . At this radius, the Keplerian velocity is  $\sim 6300 \text{ km s}^{-1}$ , implying that the full width at half maximum (FWHM) of the emission lines could reach up to twice this value. However, contributions from larger radii act to moderate this broadening.

Next, we derive the BLR response function based on the cloud positions for an inclination angle of 40 degrees, which is likely representative of NGC 5548. The resulting shape, shown in Figure 2, exhibits two distinct peaks: one at shorter distances, around  $\sim 2.6$  days, corresponding to the clouds on the same side as the observer, and the other peak arising from the clouds on the opposite side of the black hole. The shape of our response function does not perfectly match the observed one in the data from Horne et al. (2021). Their projected response from the MEMECHO software for  $H\beta$  (their Fig. 5, right panel) shows two peaks: one at  $\sim 2$  days and the second one, much smaller, at  $\sim 22$  days. Our first peak coincides quite well with their first peak but our

second peak is located closer in, at  $\sim 11$  days and it is relatively stronger than the second peak of Horne et al. (2021). However, it is noteworthy that no arbitrary parameters, such as inner or outer radii, were introduced—only global parameters were used. This lack of free parameters adds to the intrigue of the observed similarity between the modeled and real response functions.

By integrating the BLR response profile derived from the FRADO model, we calculate a mean delay of 8.101 days for a viewing angle of 30 degrees and 8.105 days for a viewing angle of 40 degrees. This delay is measured relative to the X-rays. To compare it with delays at other wavelengths, such as the commonly used  $5100 \text{ \AA}$ , it is essential to account for the net time delay between the X-rays and the specific wavelength of interest.

The measured time delay of the  $H\beta$  line relative to the  $5100 \text{ \AA}$  continuum during the 2014 campaign (January to June) was reported by Pei et al. (2017) as  $4.17^{+0.36}_{-0.3}$  days, which is shorter than predicted by the radius–luminosity relation. This  $H\beta$  delay ranks among the shortest ever recorded for NGC 5548. In contrast, the mean response function from the 1998–2001 campaign peaked around 20 days (Cackett & Horne 2006). Horne et al. (2021) later explored the nature of this shorter delay in detail, finding that the response function exhibited a secondary peak at approximately  $\sim 23$  days but began with a high value at zero time delay. Their observed map also supports the primary response originating from the near side of the BLR, facing the observer.

To compare the predicted and observed time delays, we need to add the delay of the  $5100 \text{ \AA}$  continuum relative to X-rays to the observed data. Since the exact time delay at  $5100 \text{ \AA}$  was not measured by Fausnaugh et al. (2016), we averaged their measurements around this wavelength and included the hard X-ray time delay, also provided in their study. This results in an estimated observed time delay for  $H\beta$  relative to X-rays of  $6.83 \pm 0.53$  days. Our predicted delay is slightly longer. This discrepancy may stem from the long tail in the delay, which the model accounts for but may not be fully captured in the observations. Alternatively, the delay could be shorter if there is intervening material between the black hole and the BLR, potentially shielding part of the most distant flow. Another possibility is that the dust temperature in the BLR model, as discussed by Panda et al. (2020) and Naddaf et al. (2021), differs from the assumed 1500 K.

Additionally, the model predicts an upper limit for the covering factor of the BLR. If the cloud distribution is not transparent, the region intercepts all radiation emitted within inclinations greater than the aspect ratio  $z/r$  of the cloud distribution. As shown in Figure 1, the model suggests that less than 4% of the radiation can be intercepted by the BLR, as the cloud height is generally small compared to the radius. This is notably lower than the 10% to 30% covering factor typically expected from BLRs (e.g. Baldwin et al. 1995; Korista & Goad 2019; Panda 2021; Panda et al. 2022). In contrast, the yearly variations observed in the line profile of NGC 5548 suggest that the disk can be distorted and/or precessing (e.g., Shapovalova et al. 2009, see their Fig. 2).

The distribution of BLR clouds enables us to roughly estimate the shape of the  $H\beta$  line predicted by the model. In this estimation, we neglect the vertical cloud velocities and only consider the projected rotational velocities towards the observer. The resulting line shape, shown in Figure 3, reveals a two-peak structure that is even more pronounced than that observed in the data. The FWHM from the model approaches  $8000 \text{ km s}^{-1}$ . In con-

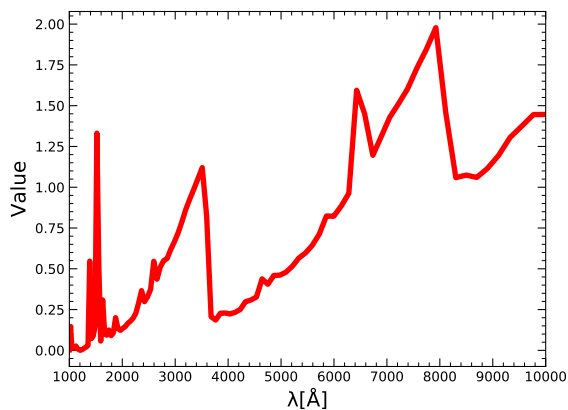


**Fig. 4.** Emissivity profile (ratio of the reprocessed to the incident continuum) of a BLR cloud for the adopted parameters:  $\log n_H [\text{cm}^{-3}] = 11$ ,  $\log L [\text{erg s}^{-1}] = 44$ , and the BLR distance of  $10^{16}$  cm.

trast, the measured FWHM for the  $H\beta$  line in 2015 from the mean spectrum was  $11,623 \pm 352 \text{ km s}^{-1}$  (Lu et al. 2022), while the FWHM measured from the RMS spectrum is slightly narrower,  $10,241 \pm 515 \text{ km s}^{-1}$ . Moreover, the FWHM values have varied in subsequent years, indicating the dynamic nature of the BLR.

#### 4.2. The BLR emissivity

To model the emission characteristics of photoionized clouds, we perform CLOUDY simulations that account for both line and continuum contributions. During our computations, we consider both line and continuum emissions, incorporating radiation from both inward and outward directions to ensure equal visibility of the illuminated and un-illuminated sides of the clouds. Among the most prominent features that emerge are the Balmer and Paschen edges, as illustrated in Figure 4. The depths of these edges are governed by the specific model parameters adopted (see, e.g., the most recent study by Pandey et al. 2023).

#### 4.3. Exemplary shape of the response function

We compute the disk response function and the combined disk-BLR response function using equations 5 and 7, respectively, and present them for nine different wavelengths in the upper and lower panels of Figure 5. As expected, the response function exhibits a bimodal shape, where the first peak corresponds to direct emission from the disk, while the second peak arises from delayed reprocessing by the BLR. This bimodality, driven by the BLR contribution, is clearly evident in the plot. Moreover, the overall time delay associated with the combined response function is significantly longer than that of the disk alone, consistent with the findings of Netzer (2022).

#### 4.4. Time delays in representative models

This paper serves as a pilot study, focusing on three distinct global setups rather than exploring the full parameter space. In this section, we assume that the source distance can be determined from its redshift, enabling a unique conversion of bolometric luminosities to fluxes. We define these setups as Model A, Model B, and Model C, each characterized by different global parameters. In Models A and C, the black hole mass is derived from observational data, whereas in Model B, it is adopted

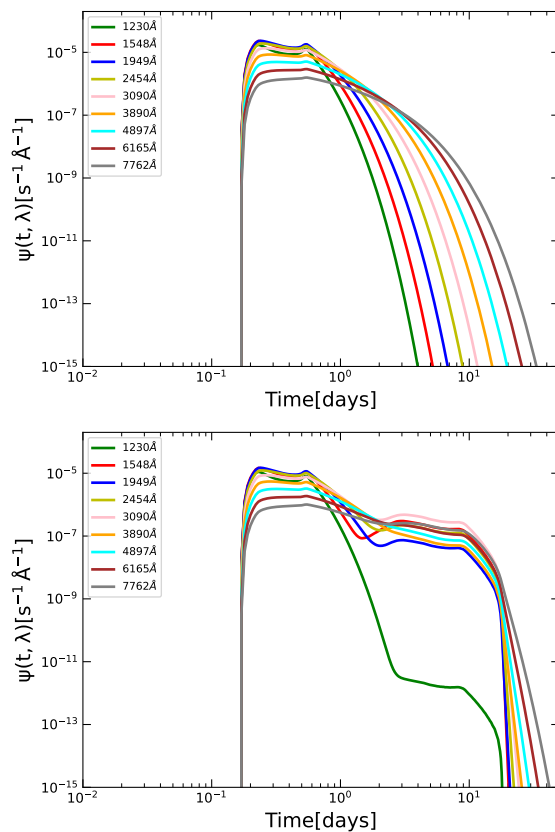


**Fig. 5.** Upper panel: Response function of the disk. Bottom panel: Combined response function of the disk and BLR. Parameters used: black hole mass =  $5.0 \times 10^7 M_\odot$ , Eddington ratio = 0.015,  $L_X = 9.52 \times 10^{43} \text{ erg s}^{-1}$ , height:  $h = 32r_g$ ,  $R_m = 90r_g$ ,  $R_{out} = 10000r_g$ , and viewing angle:  $i = 40$  degrees.

from the corresponding model reference. A detailed discussion of each model follows in the subsequent sections.

##### 4.4.1. Model A

In Model A, we minimize the number of free parameters by relying on the basic parameter values from the literature, including the black hole mass, Eddington rate, color correction, and viewing angle (see Table 1). Specifically, the adopted color correction of 2.4 comes from the studies of Kammoun et al. (2021b, 2023). The BLR model is then directly determined based on the assumed black hole mass, Eddington rate, and a fixed metallicity of 5. The resulting predictions are presented in Figure 6. Below, we outline the key advantages and limitations of this model.

Model advantages:

- three free parameters: starlight level, inner disk radius, BLR fraction
- the  $H\beta$  delay is approximately recovered
- the double peak shape is approximately recovered
- the time delay is well modeled

Model limitations:

- The optical/UV SED is inconsistent with the observed data

The discrepancy between the observed and modeled SED is substantial, differing by a factor of several, and cannot be resolved by adjusting any model parameters. Additionally, in

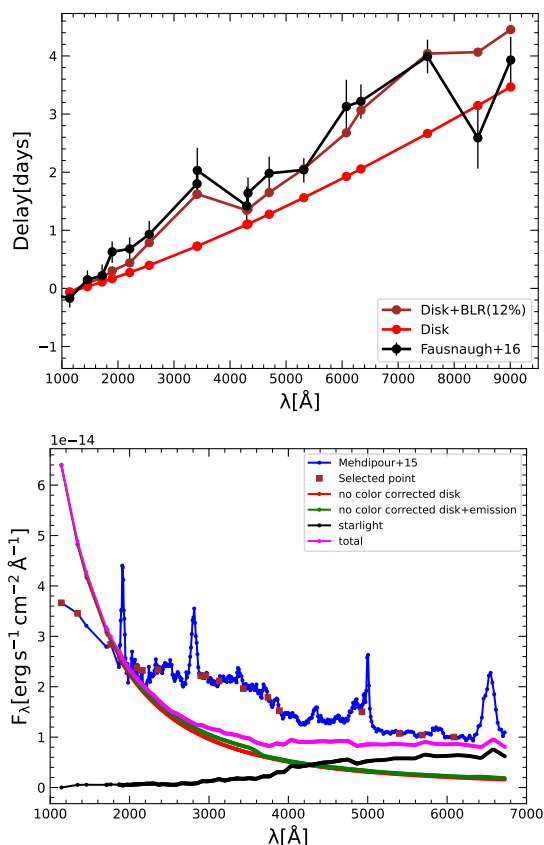


**Fig. 6. Model A.** Upper panel: The observed delay from Fausnaugh et al. (2016) is represented in black. The delay calculated from the disk response function alone is shown in red, while the delay calculated from the combined response function of the disk and BLR is shown in brown. Bottom panel: The observed SED from Mehdipour et al. (2015) is shown in blue. The disk SED is represented in red, while green illustrates the disk SED combined with the emission lines. The starlight contribution is shown in black color. The final SED, incorporating contributions from the disk, star, and emission lines, is shown in purple. The selected points used for estimating the  $\chi^2$  value are represented by brown squares. Parameters: black hole mass =  $5.0 \times 10^7 M_\odot$ , Eddington ratio = 0.02,  $L_X = 1.26 \times 44 \text{ erg s}^{-1}$ , height:  $h = 20 r_g$ ,  $R_m = 35 r_g$ ,  $R_{out} = 10000 r_g$ , color correction = 2.4, viewing angle:  $i = 40$ .

Model A, the time delay is primarily driven by the disk response, with the BLR contribution appearing only near the Balmer edge—contrary to the findings of Netzer (2022). This discrepancy arises because the disk contribution is underestimated due to the fixed color correction being set too high. While this increases the time delay by pushing the fixed-color emission outward, it simultaneously shifts the disk spectrum toward the far-UV. Consequently, we do not include the SED fit from Model A in the  $\chi^2$  minimization, as further adjustments would not improve the fit.

The starlight contribution in our decomposition is  $6.74 \times 10^{-15} \text{ erg s}^{-1} \text{ cm}^{-2} \text{ \AA}^{-1}$ , comparable to reported value of  $6.2 \times 10^{-15} \text{ erg s}^{-1} \text{ cm}^{-2} \text{ \AA}^{-1}$  (Mehdipour et al. 2015). Furthermore, this model fails to reproduce both soft and hard X-rays, as it includes only a cold disk. As a result, there is an inconsistency between the shape of the incident continuum assumed in the CLOUDY modeling and the continuum produced by the model itself.

#### 4.4.2. Model B

In Model B, we adopt the framework of Kubota & Done (2018), where the innermost part of the accretion disk is replaced by a hot corona. In our setup, the standard accretion disk extends from  $151 r_g$  to  $282 r_g$ , and we do not apply any color correction since the disk in this region remains cold. The global system parameters and the inclination angle are consistently taken from Kubota & Done (2018). The free parameters in the model were the BLR contribution,  $f_{BLR}$ , and the level of starlight. The corona height was fixed at the value of the inner radius of the corona.

The results of this model are presented in Figure 7. As in model A, we employ the same BLR response function (see Section 4.1). However, this approach may introduce minor inconsistencies due to slight differences in the black hole mass and accretion rate. While the time delay fit remains broadly satisfactory, the SED is again not well reproduced. The reduced inner disk radius results in a steep decline in the disk spectrum at shorter wavelengths.

In this configuration, the total time delay is predominantly influenced by the BLR, with only a minimal contribution from the accretion disk. Consequently, the contribution from BLR to the time delay is significantly higher than in model A. Additionally, the amount of starlight in this case is  $5.39 \times 10^{-15} \text{ erg s}^{-1} \text{ cm}^{-2} \text{ \AA}^{-1}$ , less than corresponding value in model A. The favored corona height is found to be  $43 r_g$ , consistent with the hot corona size reported in Kubota & Done (2018).

Model advantages:

- only two free parameters: starlight level, BLR fraction
- the H $\beta$  delay is approximately recovered
- the double peak shape is approximately recovered
- the time delay is reasonably well modeled

Model limitations:

- Although the high-energy portion of the SED is reasonably well recovered, this model fails to accurately fit the 3000–4000 Å wavelength range, which includes the Balmer jump, and shows some inconsistencies at longer wavelengths in the optical regime. This is related to the limited flexibility due to a small number of free parameters.

#### 4.4.3. Model C

In this model, we follow a similar approach to Model B but with considerable modifications. We allow for the variation of the radii dividing the zones. We assume that the cold outer disk is large. We also vary the warm corona parameters as well as the Eddington rate, to achieve the best fit to the broad band spectrum (including X-rays) and to time delays.

The recovered time delays from this model, along with the fitted SEDs, are displayed in the top, middle, and bottom panels of Figure 8, respectively. The Balmer edge is well reproduced in the lag-spectrum. Regarding the Paschen edge, which exhibits a pronounced dip, we do not expect this feature to be fully reproduced. As shown in Pandey et al. (2023) (see their Fig. 4), the ratio of the Balmer to Paschen jump consistently shows that the Balmer jump is usually more prominent.

Additionally, the broad-band SED is now accurately represented, with the starlight continuum at  $2.75 \times 10^{-15} \text{ erg s}^{-1} \text{ cm}^{-2} \text{ \AA}^{-1}$ , which is lower than the value of  $6.2 \times 10^{-15} \text{ erg s}^{-1} \text{ cm}^{-2} \text{ \AA}^{-1}$  reported by Mehdipour et al. (2015). We show only the uv-optical part here for better exposure of the spectral details in the bottom panel. The disk contribution to the time delay in this



model falls between the contributions in Model A and Model B. Overall, the time delay is reproduced much more accurately compared to the other two models, providing a better fit to the observed data. The contribution of the corona to the spectrum is dominating the part of the spectrum below  $\sim 2000 \text{ \AA}$ .

In conclusion, this model offers a significant improvement in both time delay and SED fitting, with a more realistic representation of the BLR contribution to the observed continuum time delays and a better overall alignment with the observed spectral features. However, challenges remain in fully capturing the Paschen edge, indicating areas for further refinement in future modeling efforts.

Model advantages:

- limited number of parameters (although larger than in model B)
- the  $H\beta$  delay is approximately recovered
- the double peak shape is approximately recovered
- the time delay is well modeled
- We successfully reproduce the Balmer jump in the observed SED, and our modeled SED is consistent with the observed spectrum.

## 5. Distance Estimation from generalized Model C

Having considered the final fit from Model C as successful, we now assess whether our model improves the determination of the Hubble constant for this source, as done by [Cackett et al. \(2007\)](#). To begin, we first explore analytical estimates and subsequently evaluate the method that should be employed for actual data fitting.

### 5.1. Analytical estimate of $H_0$

[Collier et al. \(1999\)](#) proposed a method for determining  $H_0$  based on continuum time delays, under the assumption that the inter-band time delays are a result of a classical accretion disk structure, as given by the following equation

$$H_0 = 89.6 \left( \frac{\lambda}{10^4} \right)^{3/2} \left( \frac{z}{0.001} \right) \left( \frac{\tau}{\text{day}} \right)^{-1} \left( \frac{f_\nu / \cos i}{Jy} \right)^{1/2} \left( \frac{X}{4} \right)^{4/3} \left[ \frac{\text{km}}{\text{s Mpc}} \right] \quad (10)$$

where  $\tau$  is the time delay measured at the wavelength  $\lambda$ ,  $z$  is the source redshift,  $f_\nu$  is the measured flux at the frequency  $\nu$  corresponding to the wavelength  $\lambda$ , and  $X$  is the parameter which can take value from 3 to 4.  $i$  is the viewing angle to the disk.

We can test the model using this formula, but it is important to use the disk delay rather than the total combined disk plus BLR time delay. The disk delay from Model C is 0.880 days at  $\lambda = 5100 \text{ \AA}$ . We convert the flux from [Lu et al. \(2022\)](#),  $F_\lambda = 5.22 \times 10^{-15} \text{ erg s}^{-1} \text{ cm}^{-2} \text{ \AA}^{-1}$ , to  $f_\nu = 4.590 \times 10^{-26} \text{ erg s}^{-1} \text{ cm}^{-2} \text{ Hz}^{-1}$ . Assuming an inclination angle of 40 degrees for the source and  $X = 4$ , we derive  $H_0$  of  $47.33 \text{ km s}^{-1} \text{ Mpc}^{-1}$ . This represents a considerable improvement over the value of  $H_0 = 15 \text{ km s}^{-1} \text{ Mpc}^{-1}$  obtained by [Cackett et al. \(2007\)](#) for the same source. The difference is largely due to the fact that we are using only the disk delay. If we had used the total time delay (disk + BLR) of 1.886 days, we would have obtained a much lower value of  $H_0 = 22.00 \text{ km s}^{-1} \text{ Mpc}^{-1}$ , closer to the result from [Cackett et al. \(2007\)](#).

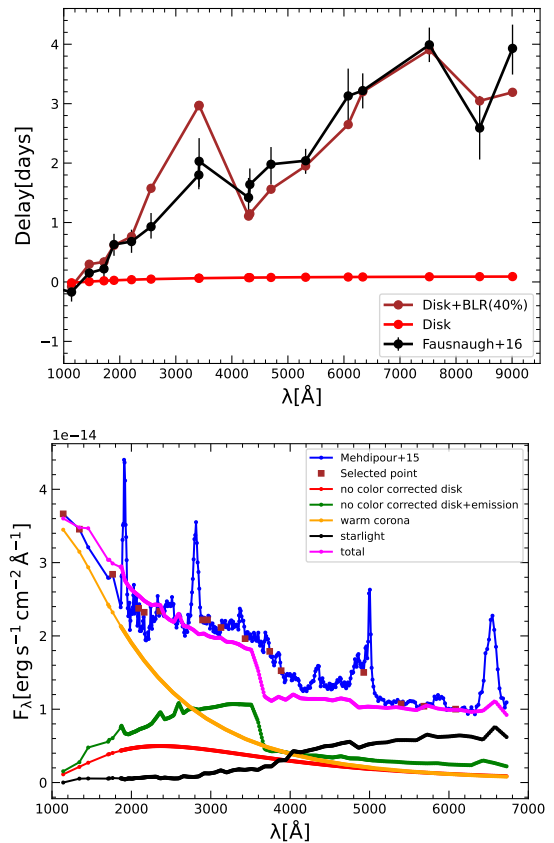


**Fig. 7. Model B.** Upper panel: The observed delay from [Fausnaugh et al. \(2016\)](#) is represented in black. The delay calculated from the disk response function alone is shown in red, while the delay calculated from the combined response function of the disk and BLR is shown in brown. Bottom panel: The observed SED from [Mehdipour et al. \(2015\)](#) is shown in blue. The disk SED is represented in red, while green illustrates the disk SED combined with the emission lines. The starlight contribution is represented in black, while the warm corona is shown in orange. The final SED, incorporating contributions from the disk, star, warm corona, and emission lines, is shown in purple. The selected points used for estimating the  $\chi^2$  value are represented by brown squares. Parameters: black hole mass =  $5.5 \times 10^7 M_\odot$ , Eddington ratio = 0.02,  $L_X = 1.247 \times 44 \text{ erg s}^{-1}$ , height:  $h = 43r_g$ ,  $R_{in} = 151r_g$ ,  $R_{out} = 282r_g$ , color correction = 1.0, viewing angle:  $i = 45$ .

### 5.2. Direct method to measure the distance to the source and $H_0$ from combined spectral and time delay fitting

The Model C in the version described in Section 4.4.3 is based on the known distance which in turn constraints the accretion rate and the bolometric luminosity. Therefore, if we indeed want to measure the distance to the source we cannot rely on quantities that were determined knowing this distance. We thus must allow the Eddington rate to cover a broad range, reflecting the possibly broad range of the luminosity distance of the source. However, we still fix the black hole mass, as it was derived from the spectral fitting (FWHM of the  $H\beta$  line) and time delay measurement, so it is not influenced by the knowledge of the luminosity distance.

In this Section, we present a series of computations using a grid of pre-selected luminosity distances. For each luminosity distance, we fit several model parameters by minimizing the  $\chi^2$  value. The parameters we vary when fitting the spectrum include the Eddington ratio ( $\dot{m}$ ), the cold disk inner radius ( $R_{in}$ ), the height of the corona ( $h$ ), the optical depth of the warm corona

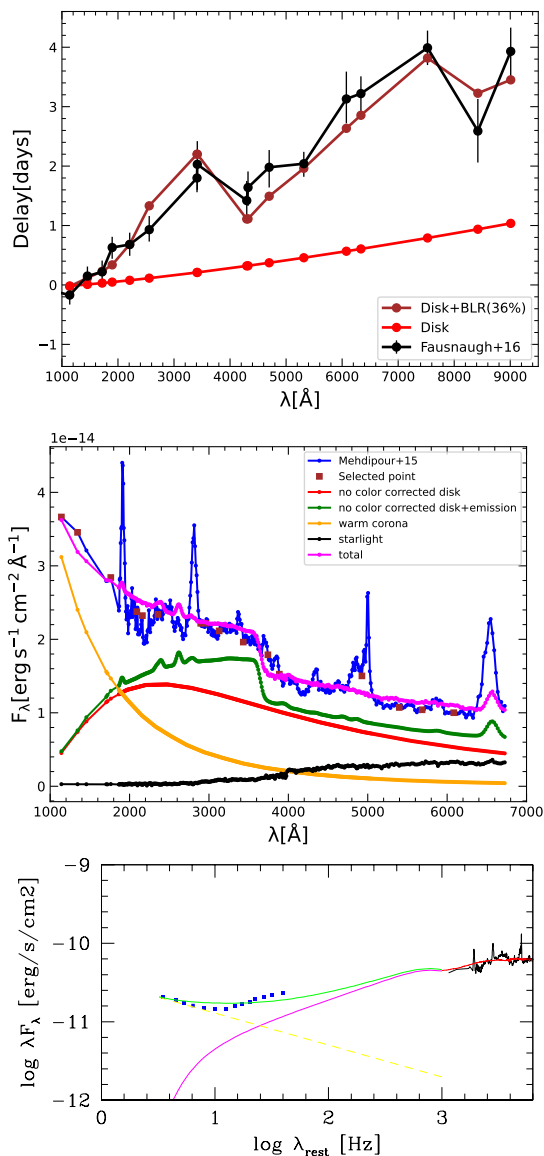


**Fig. 8.** Model C. Upper panel: The observed delay from Fausnaugh et al. (2016) is represented in black. The delay calculated from the disk response function alone is shown in red, while the delay calculated from the combined response function of the disk and BLR is shown in brown. Middle panel: The observed SED from Mehdipour et al. (2015) is shown in blue. The disk SED is represented in red, while green illustrates the disk SED combined with the emission lines. The starlight contribution is represented in black, while the warm corona is shown in orange. The final SED, incorporating contributions from the disk, star, warm corona, and emission lines, is shown in purple. The selected points used for estimating the  $\chi^2$  value are represented by brown squares. Parameters: black hole mass =  $5.0 \times 10^7 M_\odot$ , Eddington ratio = 0.015,  $L_X = 9.52 \times 10^{43}$  erg s<sup>-1</sup>, height:  $h = 32r_g$ ,  $R_{in} = 90r_g$ ,  $R_{out} = 10000r_g$ , color correction = 1.0, viewing angle:  $i = 40$ . Bottom panel: X-ray–UV–optical SED fitting. The warm corona is represented by the magenta line, the hard X-ray power law is shown in yellow, the green line represents the sum of the two, and the black line displays the optical data.

( $\tau_{op-depth}$ ), the temperature of the hot corona ( $T_e$ ), the covering factor of the BLR ( $f_{BLR}$ ), and the normalization of the starlight ( $A_{star}$ ). In order to illustrate the relative role of the delay fitting and spectral fitting, we first show results when only one type of data is used (delay or spectra), and only then we show the importance of the combined fitting.

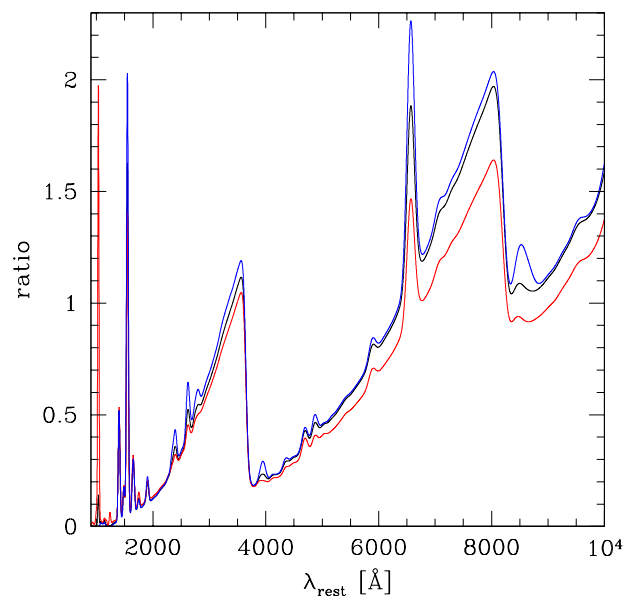


**Fig. 9.** Examples of the BLR emission profile for three values of the logarithm of the bolometric luminosity (44.0, black line), 43.8 (blue line) and 44.2 (red line) corresponding to the three values of the luminosity distance,  $D_L$ : 70, 56 and 84 Mpc.

In experiments where only the time delay is fitted, we vary only the first four parameters, keeping the remaining three fixed at the values determined by the spectral best fit, as they do not significantly influence the time delay. In the global fitting method, where both the spectra and the time delays are fitted simultaneously, we also freeze the last three parameters at their best-fit values from the spectral fitting alone. This approach is adopted because spectral fitting is computationally fast, while fitting the time delay is considerably slower, taking over an hour per model. Looking ahead, we aim to accelerate the time delay fitting code or develop a table model to improve computational efficiency.

The incident radiation in the CLOUDY computations is determined by the choice of the luminosity distance, as the incident radiation must match the observed hard X-ray flux. Therefore, for each value of the luminosity distance, we use a different spectral shape for the BLR component. Figure 9 illustrates exemplary shapes corresponding to different normalizations of the incident flux. It is important to note that the distance to the BLR and the internal parameters of the clouds remain unchanged throughout these computations.

The dependence of the BLR shape on the incident flux is not monotonic. However, the changes are relatively small, as the range of the considered flux amplitude variation is limited. It is important to emphasize that we do not modify the spectral shape of the incident radiation, as it was derived from observations rather than the model. During spectral fitting, we construct the final model spectrum based on absolute luminosity and compare it to the observed flux, taking into account the adopted distance

$$F_\lambda = \frac{L_\lambda}{4\pi D_L^2} \quad (11)$$

The value of  $\chi^2$  is calculated at several wavelengths, excluding the intense emission lines. Soft X-ray data points, taken from [Mehdipour et al. \(2015\)](#), are also included in the calculation. We assume a 10% error in the spectral fitting process. For the time delay, the  $\chi^2$  value is based on the errors complementing the time delay measurements ([Fausnaugh et al. 2016](#)).

To illustrate the roles of time delay fitting and spectral fitting, we first show the results of fitting these two types of observational data separately. The  $\chi^2$  values in the luminosity distance space for the SED-only fit are shown in the upper panel of Figure 10. The fit is not very sensitive to the adopted value of the luminosity distance,  $D_L$ . The key parameter that changes with  $D_L$  is the accretion rate. The formal minimum of  $\chi^2$  occurs at  $D_L = 50$  Mpc, with the Eddington ratio varying from  $\sim 0.005$  at  $D_L = 38$  Mpc to  $\sim 0.02$  at  $D_L = 82$  Mpc. Along with this change in the accretion rate, the corona height decreases from  $22 r_g$  to  $12 r_g$ . Additionally, the covering factor of the BLR,  $f_{BLR}$ , decreases from 0.42 to 0.30. The stellar contribution also decreases by a factor of 4 as  $D_L$  increases. Despite these variations, the optical depth of the hot corona remains unchanged at 21.5, while the electron temperature increases slightly for the two highest values of  $D_L$ , staying otherwise at  $5.97 \times 10^6$  K. Finally, the reduced  $\chi^2$  is smaller than 1, suggesting that the adopted errors can be overestimated.

Complementarily, we also fit only the delay data set in the lag-spectrum, with the corresponding sequence of  $D_L$  shown in the lower panel of Figure 10. In this case, the values of the reduced  $\chi^2$  are significantly larger. The dependence of  $\chi^2$  on  $D_L$  is relatively weak, with the minimum occurring at  $D_L = 74$  Mpc. This sequence exhibits very different properties compared to the spectral sequence. Notably, the Eddington ratio remains constant at 0.015, independent of  $D_L$ , since there is no direct coupling between the delay, the distance, and the source luminosity. The weak variation in the irradiation flux does not lead to a substantial change in the model structure.

Therefore, the combined fitting of both the SED and the time lag-spectrum is essential. Spectral fitting enforces a change in the best-fit Eddington ratio with  $D_L$ , which, in turn, affects the delay fitting. A small Eddington ratio implies a smaller source size and shorter time delays as expected from standard disk. The results of the combined fitting are shown in the upper panel of Figure 11 in luminosity distance space. Now, in the  $\chi^2$ - $D_L$  plane, each point in the sequence corresponds to the same Eddington ratio and other parameters in both the time delay and spectral fitting. The minimum occurs at  $D_L = 62$  Mpc in our grid, though the minimum is relatively shallow. The best fit for both the spectrum and the time delay at this grid is also presented in Figure 8.

The sequence shares some properties with the previously discussed separate solutions. The accretion rate predictably increases along the sequence, while the covering factor decreases. The results are weakly sensitive to the lamp height, which remains close to  $\sim 25 r_g$ , as well as to the inner radius of the cold disk, which is located at  $\sim 80 r_g$  in all fits.

This can be directly translated into the Hubble constant using the expression  $H_0 = zc/D_L$ , given that the redshift to the source is small. Thus, the same result, but as a function of the implied  $H_0$ , is shown in the lower panel of Figure 11. The distance of  $D_L = 62$  Mpc corresponds to a Hubble constant of  $79.8 \text{ km s}^{-1} \text{ Mpc}^{-1}$ . Since the minimum is shallow, the error is large, leading to our constraint of  $H_0 = 79.8_{-16.4}^{+5.5} \text{ km s}^{-1} \text{ Mpc}^{-1}$ .

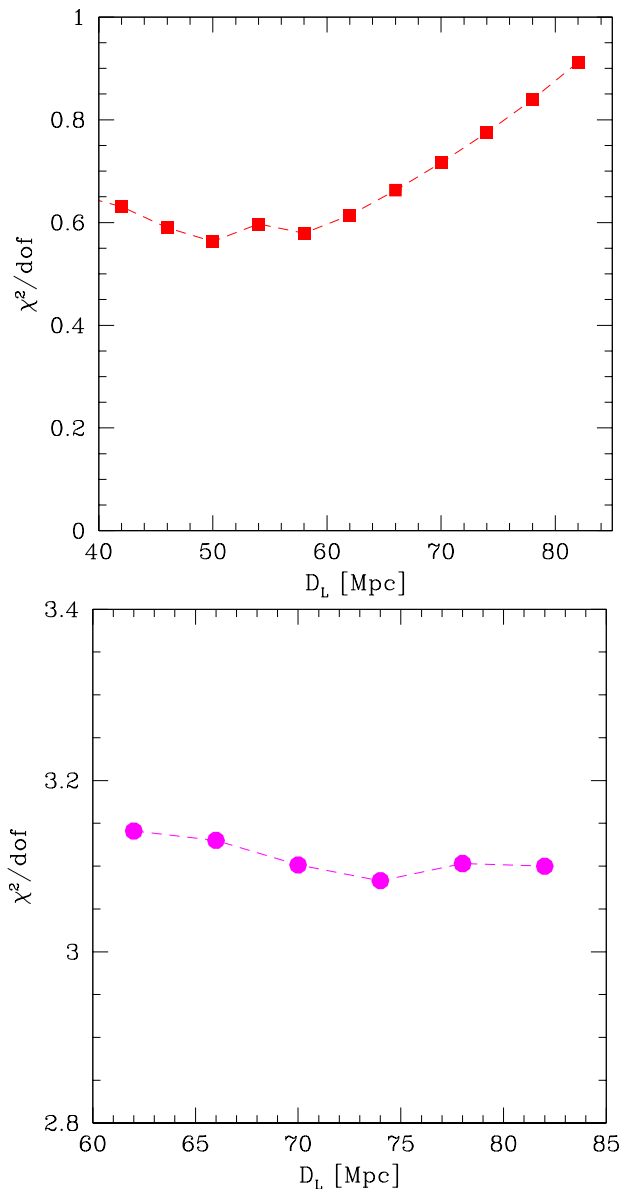


**Fig. 10.** The sequence of best fits of the spectrum (upper panel) and the delay (lower panel) as a function of the luminosity distances, marginalized for other model parameters.

Note that, in this analysis, we do not vary all the parameters involved in Model C when calculating the spectral and time delay fits, as described above. Therefore, the derived constraint should be interpreted as an indication that the methodology is working, with further progress expected to reduce the error.

The value is well within the error range of the expected values ([Abdalla et al. 2022](#); [Freedman et al. 2024](#)). The measurement error may decrease with improved modeling of the continuum in this source. Additionally, combining measurements from more sources will help further reduce the error. This value is higher than the  $47.33 \text{ km s}^{-1} \text{ Mpc}^{-1}$  obtained from the analytical formula, which suggests that the proper methodology – avoiding forced power-law solutions and the extra  $X$  parameter – is essential.

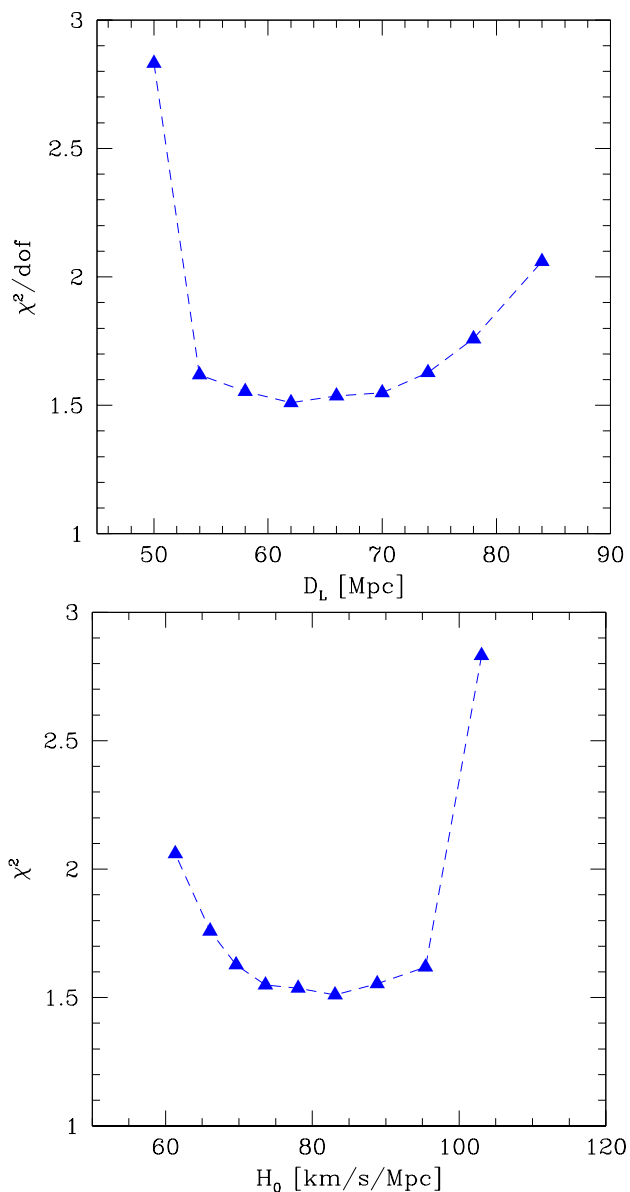


**Fig. 11.** The sequence of best fits of both the spectrum and the delay as a function of the luminosity distances (upper panel), marginalized for other model parameters. The lower panel shows the same plot as a function of the resulting Hubble constant.

## 6. Discussion

The aim of this paper is two-fold: first, to test the FRADO model for the formation of the BLR, and second, to attempt the estimation of the Hubble constant from such a self-consistent model by determining the redshift-independent distance to the source NGC 5548. While this remains a pilot study, our results demonstrate that the method holds significant potential.

The model itself involves very few parameters. The black hole mass has been fixed, and we have not yet tested its dependence on the results. However, it is worth noting that the black hole mass can be considered independent of the redshift when determined from the line shape. The key parameters – Eddington ratio, BLR contribution, and cold disk inner radius – are fitted using the observed mean spectrum and the continuum time delays measured in the continuum–RM campaign by Fausnaugh et al. (2016). The best fit favors a redshift-independent distance of 62 Mpc to the source. This distance, when converted to the Hubble

constant, implies a value of  $H_0 = 79.8^{+5.5}_{-16.4}$  km s<sup>-1</sup> Mpc<sup>-1</sup>. Additionally, the model successfully reproduces the H $\beta$  time delay. One hidden parameter in the FRADO model is the dust sublimation temperature,  $T_{\text{sub}}$ , which we adopted as 1500 K. Variations in this temperature would directly influence the favored distance, roughly following the relationship  $r \propto (T_{\text{sub}}/1500\text{K})^{-4/3}$ .

The multi-wavelength time delays in NGC 5548 have also been modeled in other studies. The original work by Fausnaugh et al. (2016), which provided the delay measurements, employed only power-law parametric modeling. More recently, Kammoun et al. (2023) fitted the NGC 5548 time delay using a new model that incorporates relativistic effects, such as the X-ray reflection component and albedo, while also exploring the influence of black hole spin and corona height. Their SED fitting yielded a higher Eddington ratio (0.05) than our solution, along with a higher black hole mass, resulting in a significantly greater bolometric luminosity for the source compared to our model. However, we cannot analyze this discrepancy in detail, as their best-fit SED was not explicitly presented. While Kammoun et al. (2023) strongly advocate for the inclusion of color correction, they do not account for the BLR contribution in their model. Notably, in both of these studies, the distance to NGC 5548 was determined using redshift measurements.

The recent study by Netzer et al. (2024) shares several key elements with our work. However, their BLR model is not based on a dynamical framework like ours, requiring additional arbitrary parameters to define the dynamics and geometry. At the same time, their study addresses important factors, such as obscuration, which are not considered in our analysis. Despite successfully fitting both the spectra and time delays for their target, Mrk 817, they did not attempt to interpret their results in terms of a redshift-independent distance or derive an estimate for the Hubble constant.

Taken together, these comparisons highlight the unique strengths of our approach. Unlike previous studies that either relied on power-law fitting, incorporated relativistic effects without addressing the BLR contribution, or did not pursue an independent distance determination, our method integrates spectral fitting and time delay modeling within a self-consistent framework. By leveraging the FRADO model, we obtained a redshift-independent distance to NGC 5548. While further refinements—such as improved continuum modeling and broader sample studies—are needed to reduce uncertainties, our results demonstrate the potential of this methodology in offering an alternative approach to cosmic distance measurements.

### 6.1. Covering factor

Although we refer to our disk-plus-BLR model as self-consistent, not all of its components are fully self-consistent yet. In principle, for a given black hole mass and Eddington ratio, the BLR covering factor should be determined by the model. Some tests of the predicted covering factor have been performed for relatively high Eddington ratios (Naddaf et al. 2023; Naddaf & Czerny 2024). However, at lower Eddington ratios, the clouds are located too close to the disk, leading to inconsistencies.

The aspect ratio of the cloud distribution, as shown in Figure 1, implies a covering factor of approximately 5%, whereas the value favored by time delay and spectral fitting is 36%. While the BLR location is well represented, the vertical motion of the clouds appears insufficient when considering only radiation pressure from dust. This suggests that line driving likely plays a role, but it is not yet included in the FRADO model.

Incorporating line driving, such as by combining FRADO with the QWIND model of [Risaliti & Elvis \(2010\)](#), is highly complex. The improved version of the QWIND software ([Quera-Bofarull et al. 2023](#)) is publicly available, providing a strong foundation for future work. However, it still lacks dust physics, which is crucial for determining the radial structure of the BLR at low luminosities. Future developments integrating these elements will be essential for achieving a fully self-consistent model.

### 6.2. FRADO vs LOC models as a method to reproduce the BLR transfer function

FRADO is a dynamical model which aims to reproduce the physical origin of the clouds, their location and their velocities. The model is not yet fully matured, but there are clear prospects for the model further development. For the dynamics, the addition of the line driving, mentioned above, should be included as its importance is increasing with the height of the clouds. Next, the emissivity of each clouds should be calculated individually, according to its location. Finally, there are two even more complex problems. One is a good realistic description of the shielding of clouds by themselves, important at low heights from the disk. The second one is determination of the density distribution of material based on thermal instability of the medium, as described already by [Krolik et al. \(1981\)](#). The wind is launched as a continuous medium, with clouds forming out of this wind in short thermal timescale.

LOC models, on the other hand, by their concept (power law distribution of clouds in radius and in density, with the limiting densities and limiting radii, and power law slopes as parameters) are better suitable for accurate matching of the line ratios in the AGN spectra. The additional parameters are still required if the distribution is flat, concentrated around the accretion disk, instead of a spherical distribution as in the original model of [Baldwin et al. \(1995\)](#). This model is mature, but its parameters must be controlled by the data. However, to derive the BLR response, additional assumptions are required. [Lawther et al. \(2018\)](#) combined spherically-symmetric approach with continuity equation to set the clod radial distribution but the authors indeed were able to determine the expected delay for all emission lines. [Korista & Goad \(2019\)](#), also using LOC model, pioneered the study of the disk continuum contamination by BLR continuum. However, it still remains to be seen if LOC models can be used in the same way as FRADO for fitting both the spectra and time delays, and for the Hubble constant determination. This was not done so far.

### 6.3. Other distance measurements to the source

The heliocentric redshift of NGC 5548 ( $z = 0.017175 \pm 2.30 \times 10^{-5}$ ; [de Vaucouleurs et al. 1991](#)) corresponds to a distance of  $79.05 \pm 5.54$  Mpc when the motion of the source is measured relative to the Cosmic Microwave Background (CMB)<sup>2</sup>. The proper motion of the source is not negligible, as indicated by the difference between its heliocentric and CMB-based velocities reported by NED ( $5149 \pm 7$  km s<sup>-1</sup> vs.  $5359 \pm 16$  km s<sup>-1</sup>).

In addition to redshift-based estimates, several independent distance measurements exist for this source. Two estimates rely on the Tully-Fisher method: an older measurement of 103 Mpc ([Bottinelli et al. 1984](#)) and a more recent one that closely aligns with the redshift-based value ( $82.2 \pm 16.4$  Mpc; [Robinson et al. 2021](#)). Meanwhile, the AGN continuum time lag method yielded

a significantly higher distance of  $341 \pm 62$  Mpc ([Cackett et al. 2007](#)). In contrast, dust reverberation mapping provided a distance of  $92.5 \pm 1.5$  Mpc ([Yoshii et al. 2014](#)), which, despite its small uncertainty, is not consistent with the redshift-based value.

Applying a velocity correction from the heliocentric frame to the CMB frame shifts the redshift from 0.01651 to 0.01721. This adjustment would, in turn, modify the our estimated value of the Hubble constant to  $83.2^{+5.7}_{-17.1}$  km s<sup>-1</sup> Mpc<sup>-1</sup>. However, given the relatively large uncertainties involved, achieving a highly precise correction for the proper motion is not crucial in this context.

### 6.4. The Hubble tension

The recent measurements of the Hubble constant generally highlight a persistent tension between early- and late-Universe determinations (see [Abdalla et al. 2022](#), for a review). A key issue in this debate is the determination of measurement uncertainties. For example, studies by [Riess et al. \(2016\)](#) and [Planck Collaboration et al. \(2016\)](#) suggest a significant discrepancy, while the baryon acoustic oscillation (BAO) measurements by [Wang et al. \(2017\)](#) are consistent with both within their reported errors. However, the overall tension remains unresolved, as indicated by the most recent results from [Riess et al. \(2024\)](#), [Uddin et al. \(2024\)](#), and [Planck Collaboration et al. \(2020\)](#).

In response to this discrepancy, several independent methods have been proposed to confirm or address the tension (e.g., see [de Jaeger et al. 2022](#); [Wong et al. 2024](#); [Trefoloni et al. 2024](#); [Liu et al. 2024](#); [Bargiacchi et al. 2025](#), for some of the latest examples). Notably, some local measurements yield lower values of  $H_0$  (e.g., [Grillo et al. 2024](#)). The latest findings from the clustering of galaxies, quasars, and Lyman- $\alpha$  forest tracers, based on the first year of observations from the Dark Energy Spectroscopic Instrument (DESI Data Release 1; [DESI Collaboration et al. 2024](#)), support a lower Hubble constant of  $68.40 \pm 0.27$  km s<sup>-1</sup> Mpc<sup>-1</sup> for a flat  $\Lambda$ CDM model, with remarkably small uncertainty. Their results, incorporating constraints from Big Bang nucleosynthesis and acoustic angular scale measurements from the CMB, suggest  $H_0 = 68.52 \pm 0.62$  km s<sup>-1</sup> Mpc<sup>-1</sup>, while a joint analysis of CMB anisotropies and CMB lensing from Planck+ACT yields  $H_0 = 67.97 \pm 0.38$  km s<sup>-1</sup> Mpc<sup>-1</sup>.

Although our method lacks the precision needed to decisively address this tension, it represents a significant improvement over the results obtained by [Cackett et al. \(2007\)](#) for this object. This progress is both substantial and encouraging.

Interestingly, distance-ladder-based measurements tend to yield higher values of  $H_0$  compared to single-step methods, with [Perivolaropoulos \(2024\)](#) reporting an average of  $H_0 = 69.0 \pm 0.48$  km s<sup>-1</sup> Mpc<sup>-1</sup>. Our target source, at a redshift of  $z = 0.01651$ , lies near the boundary of  $z \sim 0.01$ , where some studies suggest a possible transition in cosmological behavior (e.g., [Gavas et al. 2025](#); [Verde et al. 2024](#)). However, given the current uncertainties in our results, we cannot yet distinguish between competing interpretations. Future efforts should focus on reducing measurement errors and extending the analysis to AGN at both lower and higher redshifts to further explore this issue.

### 6.5. Prospects for continuum reverberation from LSST

The standard six-color photometry provided by the Legacy Survey of Space and Time (LSST), soon to be available from the Vera Rubin Observatory, may not achieve the same level of precision in time delay measurements as combined SWIFT/ground-based monitoring. However, there remain promising opportuni-

<sup>2</sup> <https://ned.ipac.caltech.edu/>

ties for detecting continuum time delays, particularly for systems with larger black hole masses with high luminosities (Pozo Nuñez et al. 2023, 2024; Panda et al. 2024).

For the most massive quasars, however, the contribution of the BLR to the observed time delay may be less significant. This is suggested by results for PG2308 + 098, a quasar with a black hole mass of  $10^{9.6\pm 0.1} M_{\odot}$ , as reported by Kokubo (2018). To better understand this effect, we can also investigate a potential scaling relation between BLR continuum contamination and emission line intensities, which may provide further insight into the role of the BLR in time delay measurements.

## 7. Conclusions

Our pilot study aimed to test the FRADO model for the BLR structure and estimate the Hubble constant based on the mean spectrum data and continuum time delay measurements for NGC 5548. The study has been highly successful, yielding several key outcomes:

- The time delay of the  $H\beta$  line is approximately recovered, even though our model does not allow for direct adjustments of the inner and outer radii of BLR. Instead, these parameters emerge naturally from computations of radiation pressure acting on dust and the dust sublimation temperature.
- By using the redshift-based distance of NGC 5548 and its known luminosity, we successfully model the overall spectrum, incorporating contributions from both the accretion disk and the BLR. Additionally, we accurately reproduce the time-delay pattern, emphasizing the crucial role played by the Balmer and Paschen edges.
- Relaxing the assumption of a known redshift-based luminosity, we model the spectrum and time-delay data across a range of Eddington ratios. For each value, we optimized the source distance, ultimately identifying a best-fit Eddington ratio and corresponding distance, which in turn provided an estimate of the Hubble constant.
- Although the uncertainty in the Hubble constant remains relatively large ( $79.8^{+5.5}_{-16.4}$  km s<sup>-1</sup> Mpc<sup>-1</sup>), our method demonstrates potential for refinement. Further improvements—both for this source and for similar determinations using other AGN with dense monitoring—could lead to significantly more precise measurements.

Our results validate the viability of using AGN continuum time delays and spectral modeling as an independent method for measuring cosmic distances and estimating the Hubble constant. While the current uncertainty is still substantial, the methodology holds promise for future applications. Expanding the sample to include additional AGNs with well-sampled continuum–RM data will be crucial for reducing uncertainties and improving the accuracy of this approach.

*Acknowledgements.* This project has received funding from the European Research Council (ERC) under the European Union’s Horizon 2020 research and innovation program (grant agreement No. [951549]). VKJ acknowledges the OPUS-LAP/GA-CR-LA bilateral project (2021/43/I/ST9/01352/OPUS 22 and GF23-04053L). MHN also acknowledges the financial support by the University of Liege under Special Funds for Research, IPD-STEMA Program. SP is supported by the international Gemini Observatory, a program of NSF NOIRLab, which is managed by the Association of Universities for Research in Astronomy (AURA) under a cooperative agreement with the U.S. National Science Foundation, on behalf of the Gemini partnership of Argentina, Brazil, Canada, Chile, the Republic of Korea, and the United States of America. BC acknowledges the support from COST Action CA21136 - Addressing observational tensions in cosmology with systematics and fundamental physics (CosmoVerse), supported by COST (European Cooperation in Science and Technology). FPN gratefully

acknowledges the generous and invaluable support of the Klaus Tschira Foundation.

## References

- Abdalla, E., Abellán, G. F., Aboubrahim, A., et al. 2022, *Journal of High Energy Astrophysics*, 34, 49
- Baldwin, J., Ferland, G., Korista, K., & Verner, D. 1995, *ApJ*, 455, L119
- Ballantyne, D. R., Sudhakar, V., Fairfax, D., et al. 2024, *MNRAS*, 530, 1603
- Bargiacchi, G., Dainotti, M. G., & Capozziello, S. 2025, *New A Rev.*, 100, 101712
- Beard, M. W. J., McHardy, I. M., Horne, K., et al. 2025, *MNRAS*, 537, 293
- Blandford, R. D. & McKee, C. F. 1982, *ApJ*, 255, 419
- Bottinelli, L., Gouguenheim, L., Patrel, G., & de Vaucouleurs, G. 1984, *A&AS*, 56, 381
- Cackett, E. M., Bentz, M. C., & Kara, E. 2021, *iScience*, 24, 102557
- Cackett, E. M. & Horne, K. 2006, *MNRAS*, 365, 1180
- Cackett, E. M., Horne, K., & Winkler, H. 2007, *MNRAS*, 380, 669
- Chatzikos, M., Bianchi, S., Camilloni, F., et al. 2023, *Rev. Mexicana Astron. Astrofis.*, 59, 327
- Clavel, J., Reichert, G. A., Alloin, D., et al. 1991, *ApJ*, 366, 64
- Collier, S., Horne, K., Wanders, I., & Peterson, B. M. 1999, *MNRAS*, 302, L24
- Czerny, B. & Hryniewicz, K. 2011, *A&A*, 525, L8
- Czerny, B., Li, Y.-R., Hryniewicz, K., et al. 2017, *ApJ*, 846, 154
- Czerny, B., Nikolajuk, M., Róžańska, A., et al. 2003, *A&A*, 412, 317
- de Jaeger, T., Galbany, L., Riess, A. G., et al. 2022, *MNRAS*, 514, 4620
- De Rosa, G., Peterson, B. M., Ely, J., et al. 2015, *ApJ*, 806, 128
- de Vaucouleurs, G. & de Vaucouleurs, A. 1972, *Astrophys. Lett.*, 12, 1
- de Vaucouleurs, G., de Vaucouleurs, A., Corwin, Herold G., J., et al. 1991, *Third Reference Catalogue of Bright Galaxies*
- DESI Collaboration, Adame, A. G., Aguilar, J., et al. 2024, *arXiv e-prints*, arXiv:2404.03002
- Edelson, R., Gelbord, J. M., Horne, K., et al. 2015, *ApJ*, 806, 129
- Fausnaugh, M. M., Denney, K. D., Barth, A. J., et al. 2016, *ApJ*, 821, 56
- Freedman, W. L., Madore, B. F., Jang, I. S., et al. 2024, *arXiv e-prints*, arXiv:2408.06153
- Gavas, S., Bagla, J. S., & Khandai, N. 2025, *Phys. Rev. D*, 111, 043516
- Grillo, C., Pagano, L., Rosati, P., & Suyu, S. H. 2024, *A&A*, 684, L23
- Guo, H., Barth, A. J., & Wang, S. 2022, *ApJ*, 940, 20
- Homayouni, Y., Trump, J. R., Grier, C. J., et al. 2019, *ApJ*, 880, 126
- Horne, K., De Rosa, G., Peterson, B. M., et al. 2021, *ApJ*, 907, 76
- Jaiswal, V. K., Prince, R., Panda, S., & Czerny, B. 2023, *A&A*, 670, A147
- Kammoun, E., Papadakis, I. E., Dovčiak, M., & Panagiotou, C. 2024, *A&A*, 686, A69
- Kammoun, E. S., Dovčiak, M., Papadakis, I. E., Caballero-García, M. D., & Karas, V. 2021a, *ApJ*, 907, 20
- Kammoun, E. S., Papadakis, I. E., & Dovčiak, M. 2021b, *MNRAS*, 503, 4163
- Kammoun, E. S., Robin, L., Papadakis, I. E., Dovčiak, M., & Panagiotou, C. 2023, *MNRAS*, 526, 138
- Kinney, A. L., Calzetti, D., Bohlin, R. C., et al. 1996, *ApJ*, 467, 38
- Kokubo, M. 2018, *PASJ*, 70, 97
- Korista, K. T., Alloin, D., Barr, P., et al. 1995, *ApJS*, 97, 285
- Korista, K. T. & Goad, M. R. 2001, *ApJ*, 553, 695
- Korista, K. T. & Goad, M. R. 2019, *MNRAS*, 489, 5284
- Kovačević, J., Popović, L. Č., & Kollatschny, W. 2014, *Advances in Space Research*, 54, 1347
- Krolik, J. H. 1999, *Active galactic nuclei : from the central black hole to the galactic environment*
- Krolik, J. H., Horne, K., Kallman, T. R., et al. 1991, *ApJ*, 371, 541
- Krolik, J. H., McKee, C. F., & Tarter, C. B. 1981, *ApJ*, 249, 422
- Kubota, A. & Done, C. 2018, *MNRAS*, 480, 1247
- Lawther, D., Goad, M. R., Korista, K. T., Ulrich, O., & Vestergaard, M. 2018, *MNRAS*, 481, 533
- Liu, T., Cao, S., Biesiada, M., Zhang, Y., & Wang, J. 2024, *ApJ*, 965, L11
- Lu, K.-X., Bai, J.-M., Wang, J.-M., et al. 2022, *ApJS*, 263, 10
- McHardy, I. M., Cameron, D. T., Dwelly, T., et al. 2014, *MNRAS*, 444, 1469
- Mehdipour, M., Kaastra, J. S., Kriss, G. A., et al. 2015, *A&A*, 575, A22
- Morgan, C. W., Kochanek, C. S., Morgan, N. D., & Falco, E. E. 2010, *ApJ*, 712, 1129
- Mudd, D., Martini, P., Zu, Y., et al. 2018, *ApJ*, 862, 123
- Naddaf, M. H. & Czerny, B. 2022, *A&A*, 663, A77
- Naddaf, M.-H. & Czerny, B. 2024, *Universe*, 10, 29
- Naddaf, M.-H., Czerny, B., & Szczerba, R. 2021, *ApJ*, 920, 30
- Naddaf, M. H., Martinez-Aldama, M. L., Marziani, P., et al. 2023, *A&A*, 675, A43
- Netzer, H. 2022, *MNRAS*, 509, 2637
- Netzer, H., Goad, M. R., Barth, A. J., et al. 2024, *ApJ*, 976, 59
- Panda, S. 2021, *A&A*, 650, A154

- Panda, S., Bon, E., Marziani, P., & Bon, N. 2022, *Astronomische Nachrichten*, 343, e210091
- Panda, S., Martínez-Aldama, M. L., Marinello, M., et al. 2020, *ApJ*, 902, 76
- Panda, S., Pozo Nuñez, F., Bañados, E., & Heidt, J. 2024, *ApJ*, 968, L16
- Pandey, A., Czerny, B., Panda, S., et al. 2023, *A&A*, 680, A102
- Pandey, A., Martínez-Aldama, M. L., Czerny, B., Panda, S., & Zajaček, M. 2024, arXiv e-prints, arXiv:2401.18052
- Papoutsis, M., Papadakis, I. E., Panagiotou, C., Dovčiak, M., & Kammoun, E. 2024, *A&A*, 691, A60
- Pei, L., Fausnaugh, M. M., Barth, A. J., et al. 2017, *ApJ*, 837, 131
- Perivolaropoulos, L. 2024, *Phys. Rev. D*, 110, 123518
- Peterson, B. M. 1993, *PASP*, 105, 247
- Peterson, B. M., Alloin, D., Axon, D., et al. 1992, *ApJ*, 392, 470
- Peterson, B. M., Balonek, T. J., Barker, E. S., et al. 1991, *ApJ*, 368, 119
- Peterson, B. M., Berlind, P., Bertram, R., et al. 2002, *ApJ*, 581, 197
- Peterson, B. M., Ferrarese, L., Gilbert, K. M., et al. 2004, *ApJ*, 613, 682
- Petrucci, P. O., Gronkiewicz, D., Rozanska, A., et al. 2020, *A&A*, 634, A85
- Planck Collaboration, Ade, P. A. R., Aghanim, N., et al. 2016, *A&A*, 594, A13
- Planck Collaboration, Aghanim, N., Akrami, Y., et al. 2020, *A&A*, 641, A6
- Pozo Nuñez, F., Bruckmann, C., Deesamutara, S., et al. 2023, *MNRAS*, 522, 2002
- Pozo Nuñez, F., Czerny, B., Panda, S., et al. 2024, *Research Notes of the American Astronomical Society*, 8, 47
- Quera-Bofarull, A., Done, C., Lacey, C. G., Nomura, M., & Ohsuga, K. 2023, *MNRAS*, 518, 2693
- Riess, A. G., Macri, L. M., Hoffmann, S. L., et al. 2016, *ApJ*, 826, 56
- Riess, A. G., Scolnic, D., Anand, G. S., et al. 2024, *ApJ*, 977, 120
- Risaliti, G. & Elvis, M. 2010, *A&A*, 516, A89
- Robinson, J. H., Bentz, M. C., Courtois, H. M., et al. 2021, *ApJ*, 912, 160
- Rokaki, E., Collin-Souffrin, S., & Magnan, C. 1993, *A&A*, 272, 8
- Rózańska, A., Czerny, B., Życki, P. T., & Pojmański, G. 1999, *MNRAS*, 305, 481
- Sergeev, S. G., Doroshenko, V. T., Golubinskiy, Y. V., Merkulova, N. I., & Sergeeva, E. A. 2005, *ApJ*, 622, 129
- Shakura, N. I. & Sunyaev, R. A. 1973, *A&A*, 24, 337
- Shapovalova, A. I., Popović, L. Č., Bochkarev, N. G., et al. 2009, *New A Rev.*, 53, 191
- Shappee, B. J., Prieto, J. L., Grupe, D., et al. 2014, *ApJ*, 788, 48
- Sunyaev, R. A. & Titarchuk, L. G. 1980, *A&A*, 86, 121
- Trefoloni, B., Lusso, E., Nardini, E., et al. 2024, *A&A*, 689, A109
- Uddin, S. A., Burns, C. R., Phillips, M. M., et al. 2024, *ApJ*, 970, 72
- Ulrich, M. H. & Boisson, C. 1983, *ApJ*, 267, 515
- Verde, L., Schöneberg, N., & Gil-Marín, H. 2024, *ARA&A*, 62, 287
- Wang, Y., Xu, L., & Zhao, G.-B. 2017, *ApJ*, 849, 84
- Wong, K. C., Dux, F., Shajib, A. J., et al. 2024, *A&A*, 689, A168
- Yoshii, Y., Kobayashi, Y., Minezaki, T., Koshida, S., & Peterson, B. A. 2014, *ApJ*, 784, L11
- Yu, Z., Martini, P., Davis, T. M., et al. 2020, *ApJS*, 246, 16